ACS Biomaterials SCIENCE & ENGINEERING
Cite This: ACS Biomater. Sci. Eng. 2019, 5, 2988−2997
Article
pubs.acs.org/journal/abseba

Top-Down Fabrication of Spatially Controlled Mineral-Gradient Scaffolds for Interfacial Tissue Engineering

Alexander J. Boys,[†] Hao Zhou,[†] Jordan B. Harrod,[‡] Mary Clare McCorry,[‡] Lara A. Estroff,[*,†,§] and Lawrence J. Bonassar[*,‡,∥]

[†]Department of Materials Science and Engineering, Cornell University, Ithaca, New York 14853, United States
[‡]Meinig School of Biomedical Engineering, Cornell University, Ithaca, New York 14853, United States
[§]Kavli Institute for Nanoscale Science at Cornell, Cornell University, Ithaca, New York 14853, United States
[∥]Sibley School of Mechanical and Aerospace Engineering, Cornell University, Ithaca, New York 14853, United States

Supporting Information

ABSTRACT: Materials engineering can generally be divided into "bottom-up" and "top-down" approaches, where current state-of-the-art methodologies are bottom-up, relying on the advent of atomic-scale technologies. Applying bottom-up approaches to biological tissues is challenging due to the inherent complexity of these systems. Top-down methodologies provide many advantages over bottom-up approaches for biological tissues, given that some of the complexity is already built into the system. Here, we generate interfacial scaffolds by the spatially controlled removal of mineral content from trabecular bone using a chelating solution. We controlled the degree and location of the mineral interface, producing scaffolds that support cell growth, while maintaining the hierarchical structure of these tissues. We characterized the structural and compositional gradients across the scaffold using X-ray diffraction, microcomputed tomography (μCT), and Raman microscopy, revealing the presence of mineral gradients on the scale of 20−40 μm. Using these data, we generated a model showing the dependence of mineral removal as a function of time in the chelating solution and initial bone morphology, specifically trabecular density. These scaffolds will be useful for interfacial tissue engineering, with application in the fields of orthopedics, developmental biology, and cancer metastasis to bone.

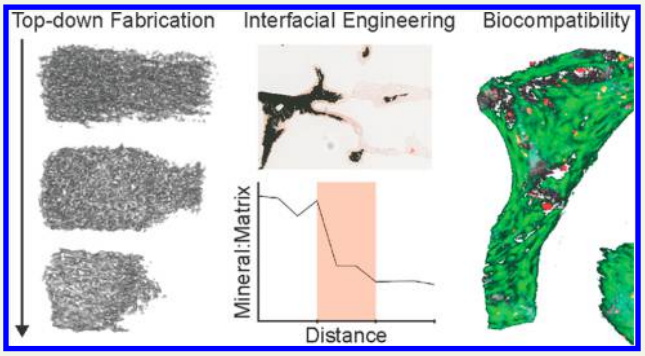

KEYWORDS: *interface, enthesis, bone, demineralization*

INTRODUCTION

Methodologies for engineering complex materials systems are often divided into "top-down" and "bottom-up" approaches. Bottom-up approaches, involving the synthesis of a material beginning at the molecular or even the atomic scale, provide a high degree of control over the final system. Current efforts in materials science and biomedical engineering generally focus on bottom-up approaches, given recent advances in materials fabrication, polymer synthesis, and other nanoscale systems.[1−3] Despite the advantages to these bottom-up systems, generating the hierarchy necessary for recapitulating tissue structure and function can be challenging. Currently, no biological scaffolds produced from a bottom-up approach have successfully recapitulated the complex structure of bone, let alone soft tissue-to-bone interfaces. Top-down approaches have been utilized throughout human history and in biomedical engineering. For example, decellularized tissue, like the intestinal submucosa, has been utilized as a tissue graft in various applications,[4−7] and demineralized bone has been used as a void filler and as a biomaterial in other applications.[8,9] Here, we develop a method for spatially controlled demineralization of decellularized bone to generate soft tissue-to-bone interfaces for tissue engineering.

Understanding the hierarchical structure of soft tissue-to-bone interfaces is critical for engineering complex, multiscale materials to match the physical and chemical properties of native tissue interfaces.[10−12] These interfaces link soft tissue with trabecular bone through multiple interfacial regions. Trabecular bone is a hierarchically structured tissue consisting at the nanoscale of oriented collagen fibrils intercalated with platelets of mineral oriented along the axis of the fibril.[13−15] This mineral is primarily poorly crystalline carbonated hydroxyapatite. At a larger scale these fibrils are arranged into lamellar sheets, which are wrapped circumferentially around a network of struts that make up the bulk of trabecular bone.[13,14] The organization of the soft tissue of these regions varies depending on the particular interface but generally consists of oriented collagen. The interface between soft tissue

Received: February 4, 2019
Accepted: May 7, 2019
Published: May 7, 2019

DOI: 10.1021/acsbiomaterials.9b00176
ACS Biomater. Sci. Eng. 2019, 5, 2988−2997

and bone consists of a series of intermediate regions, typically unmineralized cartilage/fibrocartilage, mineralized cartilage/fibrocartilage, and a thin layer of dense bone, all of which are centrally coupled by a mineral gradient.[10−12,16,17] This gradient dictates the interface between these hard and soft tissues.

Soft tissue-to-bone interfaces exist throughout the human body. Most notably, these interfaces are present at the ends of ligaments and tendons and between cartilage and bone. In all these cases, the interface mechanically mediates a multiple order of magnitude transition in stiffness.[16,18,19] For ligaments and tendons, the function of the interface is primarily mechanical, transitioning the tensile strains experienced in the ligament into the bone to allow for stabilization and movement. The function of the interface between cartilage and bone varies depending on the location. The osteochondral interface plays a mechanical role, linking cartilage to bone and providing an anchor for articulation within the knee joint. Other cartilage-to-bone interfaces are relevant to development, such as the growth plate and the interface present during endochondral ossification.[10,11,20] These interfaces can also act as loci for cancer metastasis to bone.[21] The pervasiveness of interfacial tissue systems throughout biological fields highlights the need for a generalizable scaffold system.

Development of interfacial tissue engineered scaffolds is important for the production of implants as well as the study of different native interfaces,[10−12,16,17] as a native-like scaffold would provide access to studying the effects of scaffold composition on cell behavior, in both healthy and pathological models.[22] Recent reviews have described the fabrication of interfacial scaffolds, which can typically be classified as graded scaffolds, consisting of multiple delineated regions, and gradient scaffolds, utilizing a continuous change in composition and/or structure.[10,11,17] Graded scaffolds[23] can precisely reproduce the relative mechanical properties across soft tissue-to-bone interfaces but may suffer from a lack of continuity between regions. Cell-based, tissue engineering approaches have shown success in generating morphologically accurate interfacial constructs.[24] As with many cell-based approaches, however, careful timing would be ultimately required to implant these scaffolds due to long culture times. Production of interfacial scaffolds using materials-based fabrication methods has generated constructs that appear morphologically similar to soft tissue-to-bone interfaces,[25] but these scaffolds do not possess the regional composition observed in native interfaces as of yet. Other bottom-up approaches have resulted in scaffolds lacking hierarchical structure or proper compositional aspects (e.g., low mineral concentration).[26,27] Gradient scaffolds have typically been produced using a bottom-up approach by growing mineral inside of a soft scaffold or mixing mineral into a soft material.[26,28] For example, a mineral gradient was formed on a polymer nanofiber scaffold by partially submerging a portion of the scaffold in a solution containing the precursor ions for apatitic mineral.[26] The top point of contact between the solution and the scaffold was continually increased over the mineral growth period, thereby generating a mineral gradient. Such scaffolds, however, which consist of calcium phosphate mineral grown on the exterior of polymer fibers, lack the hierarchical structure of bone. Other scaffolds with mineral gradients have been fabricated using complex diffusion systems, but these scaffolds also lack the hierarchical structure of bone.[27,29] Although these approaches are encouraging, collectively they point to the need for methods to produce hierarchical scaffolds with graded structure and composition to more accurately mimic those seen in native interfaces.

We have chosen to approach this problem of generating a mineral gradient using spatially controlled mineral *removal* from bone. Demineralization is commonly used in biology and biomedical engineering to prepare samples for histological analysis. Further, powdered, demineralized bone has been used as a void filler during surgery.[8,9] For these applications, demineralization is often accomplished using strong demineralizing agents like hydrochloric acid or formic acid. These agents risk damaging the underlying protein matrix during demineralization, thereby eliminating the hierarchical structuring inherent to tissue. Demineralization using a chelator, ethylenediaminetetraacetic acid (EDTA), has been shown to leave the protein matrix intact.[30] To the best of our knowledge, no studies have examined methods for spatially controlled demineralization, regardless of demineralization agent.

In this study, we demonstrate the fabrication of a cell-seedable scaffold with an apatitic mineral gradient possessing the inherent hierarchical structure of trabecular bone. These scaffolds were generated using a top-down approach, by removing the mineral content from decellularized bone. The resulting scaffold was demonstrated to contain structural and compositional gradients and an intact fibrillar collagen structure. Such scaffolds are useful for generating tissue engineered interfaces with application in orthopedics, developmental studies, and cancer research.

MATERIALS AND METHODS

Bone Plug Decellularization. Trabecular bone biopsies were extracted and decellularized as previously described.[31,32] Briefly, bone biopsies were explanted from 1−3 day old neonatal bovine distal femurs (Gold Medal Packing, Inc., Rome, NY) using a 6 mm diameter coring bit and sectioned into 10 mm long cylinders. Cellular debris and bone marrow were removed from biopsies by rinsing them with a high velocity stream of deionized water (∼140 mL/s through a 5 mm diameter nozzle), followed by sequential soaks of 0.1 w/v% ethylenediaminetetraacetic acid (EDTA) (TCI, Tokyo, Japan) in phosphate buffered saline (PBS) (Corning, Manassas, VA) for 1 h, hypotonic buffer (10 mM Trizma base (TCI, Tokyo, Japan), 0.1 w/v % EDTA in PBS) at 4 °C for 24 h, and detergent (10 mM Trizma base, 0.5 w/v% sodium dodecyl sulfate (SDS) (Sigma, St. Louis, MO) in PBS) at 4 °C for 24 h. Following washes, biopsies were rinsed 7 times with PBS and frozen.

Partial Demineralization. Bone biopsies were skewered on a 20 gauge surgical needle and partially suspended in a bath containing 9.5 w/v% EDTA in PBS solution (pH = 7.4) for demineralization.[30] The EDTA solution was gently stirred, avoiding the formation of a vortex. The bone plugs were collected at time points of 3, 4, 4.5, 5, 6, and 12 h. The partially demineralized bone plugs were washed with deionized water 5 times and frozen (Figure 1, Figure S1).

X-ray Computed Tomographic Analysis. Mineral content in bone scaffolds was analyzed using microscale X-ray computed tomography (μCT) at either a ∼15 μm voxel resolution (Xradia Zeiss VersaXRM-520, Zeiss, Oberkochen, Germany), or a 50 μm voxel resolution (GE eXplore CT-120 microCT, GE Healthcare, Chicago, IL). Higher resolution data were processed using Avizo Fire software (Version 8.1.1) to visualize the mineral profile and the microstructure of the trabecular bone. Lower resolution μCT data were processed using FIJI[33] to examine the demineralization process. To analyze these data, μCT stacks containing interfacial scaffolds were converted to 8-bit images. These stacks were normalized to the sample holder, a gridded paper box. To eliminate variations in the sample holder material, 30 randomly chosen voxels were averaged, and each voxel in the stack was divided by this number. The normalized data were thresholded using an empirically derived value

DOI: 10.1021/acsbiomaterials.9b00176
ACS Biomater. Sci. Eng. 2019, 5, 2988−2997

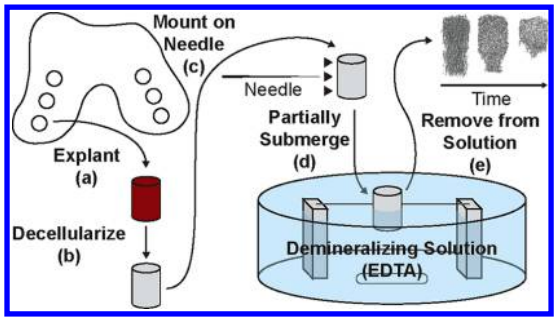

Figure 1. Schematic of process for forming mineral gradient in bone scaffolds. (a) Bone biopsies are explanted from bovine condyles using a coring bit. (b) Cartilage and bone marrow are removed from biopsies, and biopsies are decellularized. (c) Biopsies are mounted on a needle. Mounting location determines location of demineralization front. (d) Bone biopsies are partially submerged in a demineralizing solution to immediately below mounting location. (e) Biopsies are removed from demineralizing solution, where time in the solution dictates the morphology of the resulting interfacial scaffold.

of 16 (from an 8-bit image), resulting in a binary image of mineralized tissue and other contents of the stack. Each scaffold was segmented from this stack by cropping around the individual scaffold and in all three dimensions. The trabecular density was determined by taking the average number of mineralized voxels from the first 10 full slices of the mineralized end of the scaffold. The number of mineral voxels was counted for the whole stack. The length of each scaffold was determined (Supporting Information, Figure S2). The fractional demineralized content was calculated by dividing the number of mineral voxels within the whole stack by the length of the scaffold. These data were processed in MATLAB to find the relationship between the fractional demineralized content, trabecular density, and time. A first order surface was fitted to the data points using the Curve Fitting Tool (cftool) package.

Powder X-ray Diffraction. X-ray diffraction (pXRD) was used to determine the relative mineral portion per quarter moving axially along the bone plug. Four partially demineralized bone scaffolds were lyophilized and quartered perpendicular to the axis, moving from mineralized to demineralized portions of the scaffold. Corresponding quarters from the four bone scaffolds were ground under liquid nitrogen using a mortar and pestle. The four powders were analyzed with pXRD using a Bruker D8 Advance ECO powder diffractometer (Bruker, Billerica, MA). The X-ray exposures were taken at a distance of 250 mm, and at 40 kV and 25 mA, with Cu Kα radiation with a detector slit opening of 9 mm. The XRD data were processed using MATLAB and Microsoft Excel. This experiment was performed four times to determine consistency.

Histology. Partially demineralized bone scaffolds were fixed, dehydrated, embedded in poly(methyl methacrylate) (PMMA), sectioned to a 10 μm thickness, and stained with Von Kossa and methyl green pyronin to visualize mineral. Other bone scaffolds were fixed, decalcified, dehydrated, embedded in paraffin, sectioned to a 4 μm thickness, and stained. Hematoxylin and eosin (H&E) and Picrosirius Red with hematoxylin were used to show collagenous matrix in trabecular bone and the result of decellularization. Sections were imaged using an Aperio Scanscope slide scanner (Aperio Technologies, Inc., Vista, CA) under bright-field. Picrosirius Red stained slides were also imaged under cross-polarizers with a Nikon Eclipse TE2000-S microscope (Nikon Instruments, Melville, NY) and a SPOT RT camera (Diagnostic Instruments, Steriling Heights, MI) to view the alignment of collagen fibrils after demineralization.

Raman Microscopy. Raman microscopy was performed on a PMMA embedded sample using a WiTec Alpha300R confocal Raman microscope. Data were collected using a 532 nm laser at 30 mW of power through a 50× objective (Zeiss LD EC Epiplan-Neofluor Dic 40x/0.55). Spectra were collected in 10 μm increments as line scans across the interface between mineralized and demineralized tissue within individual trabeculae in the transition zone between the fully mineralized and fully demineralized ends of the bone plug. Each spectrum is an average of 3 accumulations with an integration time of 8 s. For analysis, data were analyzed in MATLAB, using the ratio of peak intensities for 957:1673 cm^{-1} to determine the mineral:matrix ratio.[34] The results at this peak ratio were also compared to the ratio of the peak intensities for 428:1673 cm^{-1}.

Mesenchymal Stem Cell (MSC) Seeding. To assess the ability of scaffolds to support cells, partially demineralized scaffolds were seeded with mesenchymal stem cells (MSCs). MSCs were isolated from trabecular bone marrow of 1−3 day old neonatal bovine distal femurs. Briefly, the trabecular region of the femur was washed with heparin supplemented media, and the extract solution was centrifuged

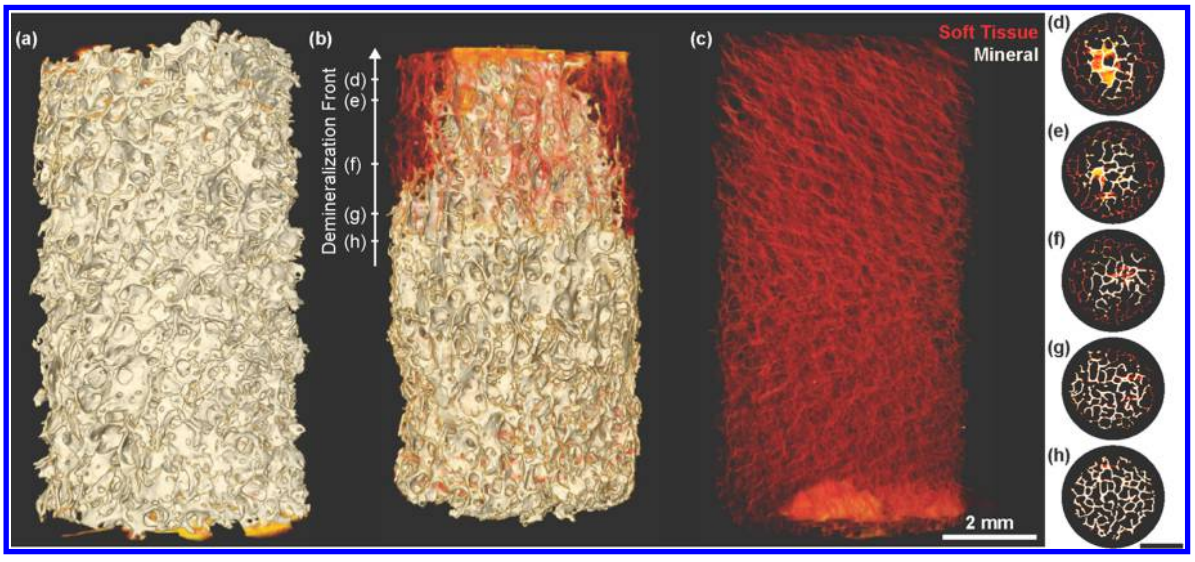

Figure 2. X-ray μCT of interfacial scaffolds showing demineralization front morphology. High densities are shown in white (mineral), and lower densities are shown in yellow and red (collagen). (a) Fully mineralized bone biopsy prior to submersion in demineralization solution. (b) Interfacial scaffold after half submersion for 4.5 h in demineralization solution. Demineralization front forms conical profile as demineralization progresses. (c) Fully demineralized bone biopsy. (d−h) Single slices from μCT of part b. Hash marks on "Demineralization Front" arrow in (b) indicate the approximate locations of each slice.

DOI: 10.1021/acsbiomaterials.9b00176
ACS Biomater. Sci. Eng. 2019, 5, 2988−2997

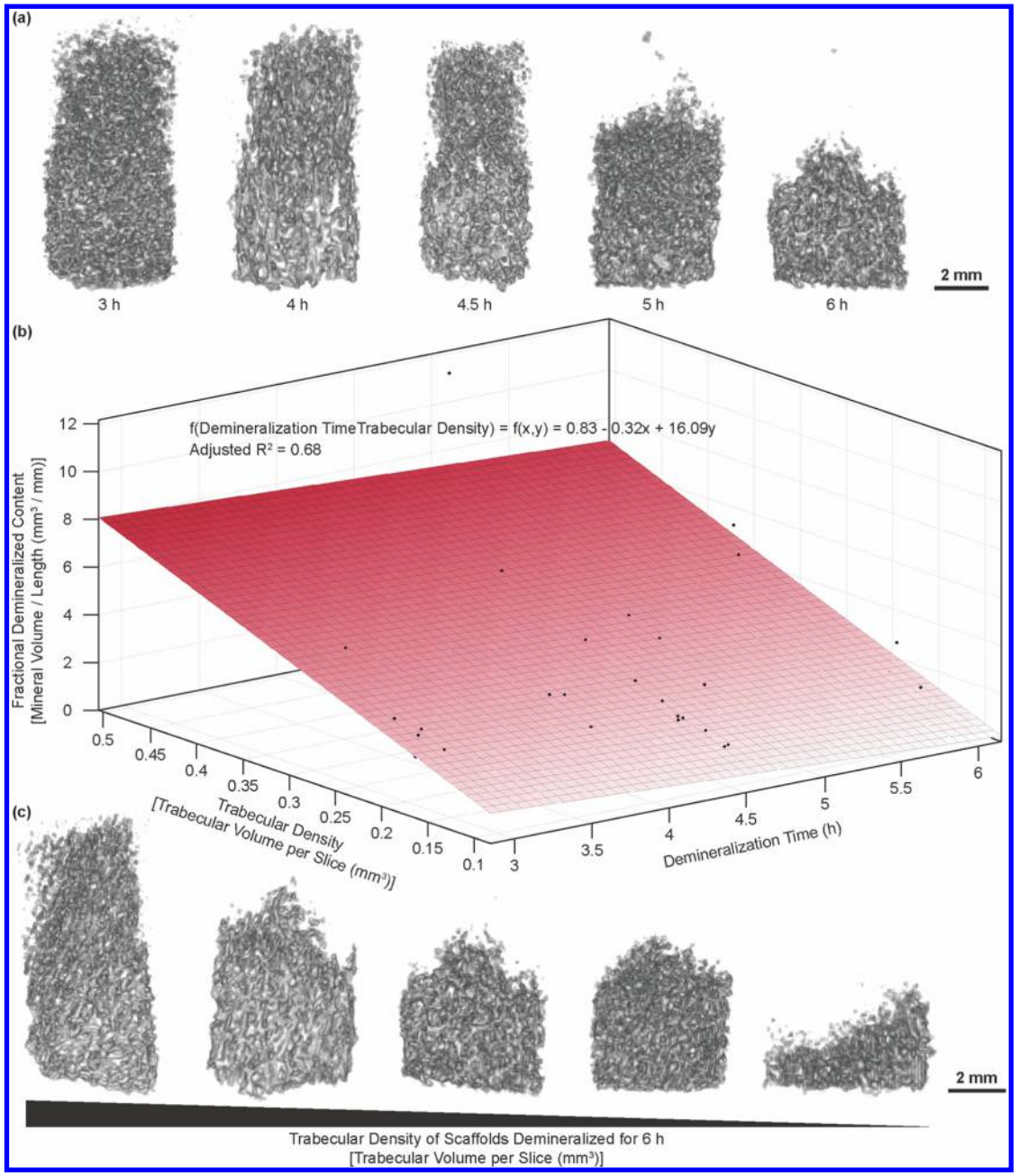

Figure 3. (a) Demineralization morphology progression for time points at a trabecular density between 0.2 and 0.25 mm^3. (b) Plot showing relationship of fractional demineralized content to time to trabecular density with accompanying fitted surface. (c) Resulting morphology of demineralizing bone scaffolds at 6 h, shown as a function of trabecular density.

at 300 × *g*. Pelleted cells were plated on culture flasks, and the nonadherent cell population was washed off after 48 h. Isolated MSCs were plated at a cellular density of 2000 cells/cm^3 and expanded to passage 2 in an expansion medium including Dulbecco's modified Eagle's medium without sodium pyruvate (DMEM) (Corning, Manassas, VA), 10% fetal bovine serum (FBS) (Gemini Bio-Products, West Sacramento, CA, 1 ng/mL basic fibroblast growth factor (bfGF) (BD Biosciences, Franklin Lakes, NJ), and 100 IU/mL penicillin.

Bone biopsies used for viability testing were cut in half along the axis prior to demineralization. These samples were skewered halfway along the axis of the sample and submerged in the demineralizing solution for 4.5 h. After partial demineralization, bone scaffolds were soaked in 70% ethanol for 1.5 h, washed in PBS, and soaked in an osteogenic media containing minimum essential medium-α (MEM-α) (ThermoFisher, Waltham, MA), 10% FBS, 100 IU/mL penicillin, 2 mM L-glutamine (VWR, Brooklyn, NY), 0.1 μM β-glycerolphosphate (MP, Santa Ana, CA), 50 μM ascorbic acid, and 0.1 μM dexamethasone. Bone scaffolds were seeded as previously described.[32] Briefly, bone scaffolds were skewered and suspended in a spinner flask. The flask was filled with 150 mL of osteogenic media containing 500 000 cells/bone scaffold and stored in an incubator for 48 h. Following seeding, scaffolds were transferred into osteogenic media for 3 days of static culture.

To determine the viability of cellular populations after seeding, live/dead stains were performed on bone. Briefly, seeded bone scaffolds were transferred from culture media to dye solution at 1 mL PBS:1 μL calcein AM:1 μL ethidium homodimer (Life Technologies Corporation, ThermoFisher, Waltham, MA), and left for 30 min. Samples were stored in PBS for at least 5 min before imaging. Imaging was performed using a Zeiss LSM 710 AxioObserver using a C-Apochromat 10×/0.45 W objective. Images consisted of 3 channels: the first channel for ethidium homodimer had an excitation

DOI: 10.1021/acsbiomaterials.9b00176
ACS Biomater. Sci. Eng. 2019, 5, 2988−2997

wavelength of 561 nm and a detection range of 582−741 nm, the second channel for calcein AM had an excitation wavelength of 488 nm and a detection range of 510−741 nm, and third channel for reflectance had an excitation wavelength of 488 nm and a detection range of 480−497 nm. Images were collected every 750 μm moving across the bone plugs, beginning approximately ∼1 mm from the beginning and ending ∼1 mm from the end of the bone plug. Slice thicknesses were ∼250 μm. Live/dead counting was performed in FIJI.[33] Data were analyzed using Microsoft Excel. Confocal z-stacks were also collected. The z-stacks taken from the ends of the bone plugs consist of 25 slices over 193.2 μm. The z-stack collected from the center of the bone plug consisted of 80 slices over 478.0 μm. Images were compiled using Zeiss ZEN 2.3 (blue edition).

Additional samples were cultured for 4 days after seeding to image the MSC-deposited matrix. These samples were prepared for sectioning and stained with H&E, as above.

RESULTS

A spatial gradient in mineral was generated in bone scaffolds through half submersion in an EDTA solution (Figure 1, Figure S1). Analysis using μCT confirmed the removal of mineral as a function of time (Figure 2, Figure S3, Movie 1). In accordance with typical diffusion patterns, mineral removal progressed from the end and sides of the scaffold, which were exposed to solution. Minimal demineralization was observed at 3 h, while at 4 h, the sides and end of scaffolds began to show the presence of demineralized collagen (Figure S3). After 4.5 h, this exposure pattern generated a conical mineral profile (Figure 2b,d−h, Movie 1).

The portion of the scaffold exposed to EDTA appeared to be entirely demineralized at 5 h, and the demineralization front began to progress into the portion of the bone scaffold that was not submerged at 6 h (Figure 3a). By 12 h, the bone scaffolds were generally observed to be entirely demineralized, with some containing a small core in the unsubmerged portion of the scaffold (Figure S3). To confirm the degree of control over the demineralization front location, scaffolds were also submerged up to a quarter and up to three-quarters of the scaffold, finding that the demineralization front progressed in a similar manner (Figure S4).

Variation in the demineralization progression was qualitatively observed to be dependent on the porosity, or, inversely, on the trabecular volume of the scaffolds, through analysis of μCT data. To confirm this speculation, the average trabecular density was calculated from the mineralized portion of each scaffold. This density was calculated as the average number of mineralized voxels over the first 10 slices from the mineralized end of the scaffold. The total mineral volume per unit length or fractional demineralized content was plotted as a function of trabecular volume and time. A first order surface was fitted to these data, finding an adjusted R^2 value of 0.68 (Figure 3b−d, and Figures S5 and S6). One sample that had been demineralized for 4.5 h became fully demineralized over this time period. This sample was not included in the analysis, as the trabecular volume could not be reliably calculated due to the lack of mineral. While the bone biopsies follow the same general trend in demineralization, the trabecular volume dictates the state the sample reaches after a given time point (Figure 3e,f). Of the 8 partially demineralized scaffolds at the 6 h time point, 6 show the expected trend in morphology, following the adjusted R^2 value of 0.68 from the fitted surface (Figure 3b).

To confirm the mineral distribution across the scaffold, pXRD was performed. For this analysis, four bone scaffolds were divided axially into quarters, and the corresponding quarters of these scaffolds were cryo-fractured and mixed together. Powder X-ray diffraction showed a decrease in the intensity of characteristic carbonated apatite peaks (∼26° and ∼32°) progressing from the mineralized end of the bone scaffold to the demineralized end (Figure 4). Further, this

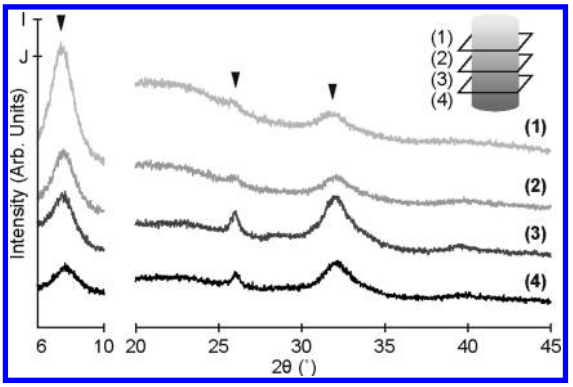

Figure 4. Representative diffraction patterns from pXRD analysis of quartered scaffolds (n = 4). (1−4) Patterns moving from demineralized (1) to mineralized (4) end of scaffold. Patterns from 6° to 10° and from 20° to 45° are scaled to I and J, respectively.

analysis confirms that the EDTA does not affect the mineral type, maintaining mineral within the scaffold as carbonated apatite.[35] A peak with increasing intensity moving from the mineralized to demineralized end of the scaffold was also observed at a 2θ of 8° (Figure 4). This peak is associated with the triple helical structure of collagen.[35]

Histological analysis was used to assess changes in the microstructure of the bone matrix in the scaffold as a function of demineralization. Hematoxylin and eosin staining shows successful decellularization and maintenance of the protein content in the scaffolds (Figure 5a). Analysis of scaffolds through Von Kossa staining demonstrates that demineralization occurs from the outside of the trabecular struts into the interior. Phosphate staining, relating the mineral content, can be observed in the cores of individual trabeculae located within the transition zone from the mineralized to demineralized ends of the bone plug (Figure 5b). Picrosirius Red staining confirms that the fibrillar structure of the collagen is not altered by the demineralization protocol (Figure 5c). Picrosirius Red stain through cross-polarizers reveals differences in coloration between the mineralized and demineralized ends of the scaffold (Figure 5d). Changes in color and intensity of Picrosirius Red stains under cross-polarizers have been shown to relate to changes in collagen fibril orientation and diameter.[36−38] Collagen appeared redder in demineralized regions of the scaffolds (Figure 5d1) and greener in mineralized areas (Figure 5d2).

The μCT, pXRD, and histology data confirm a structural gradient, on the order of hundreds to thousands of microns, moving from the mineralized to demineralized ends of the bone plugs. From the Von Kossa staining, we noted a transitional zone between the two regions in which individual trabeculae possess apparent mineral gradients on a much smaller length scale (Figure 6a). To semiquantitatively measure these compositional gradients, we used Raman microscopy on PMMA embedded tissue. This analysis revealed a ∼20−40 μm gradient in the mineral:matrix ratio ($\nu_1PO_4^{3-}$:amide I) within the individual trabecular located

DOI: 10.1021/acsbiomaterials.9b00176
ACS Biomater. Sci. Eng. 2019, 5, 2988−2997

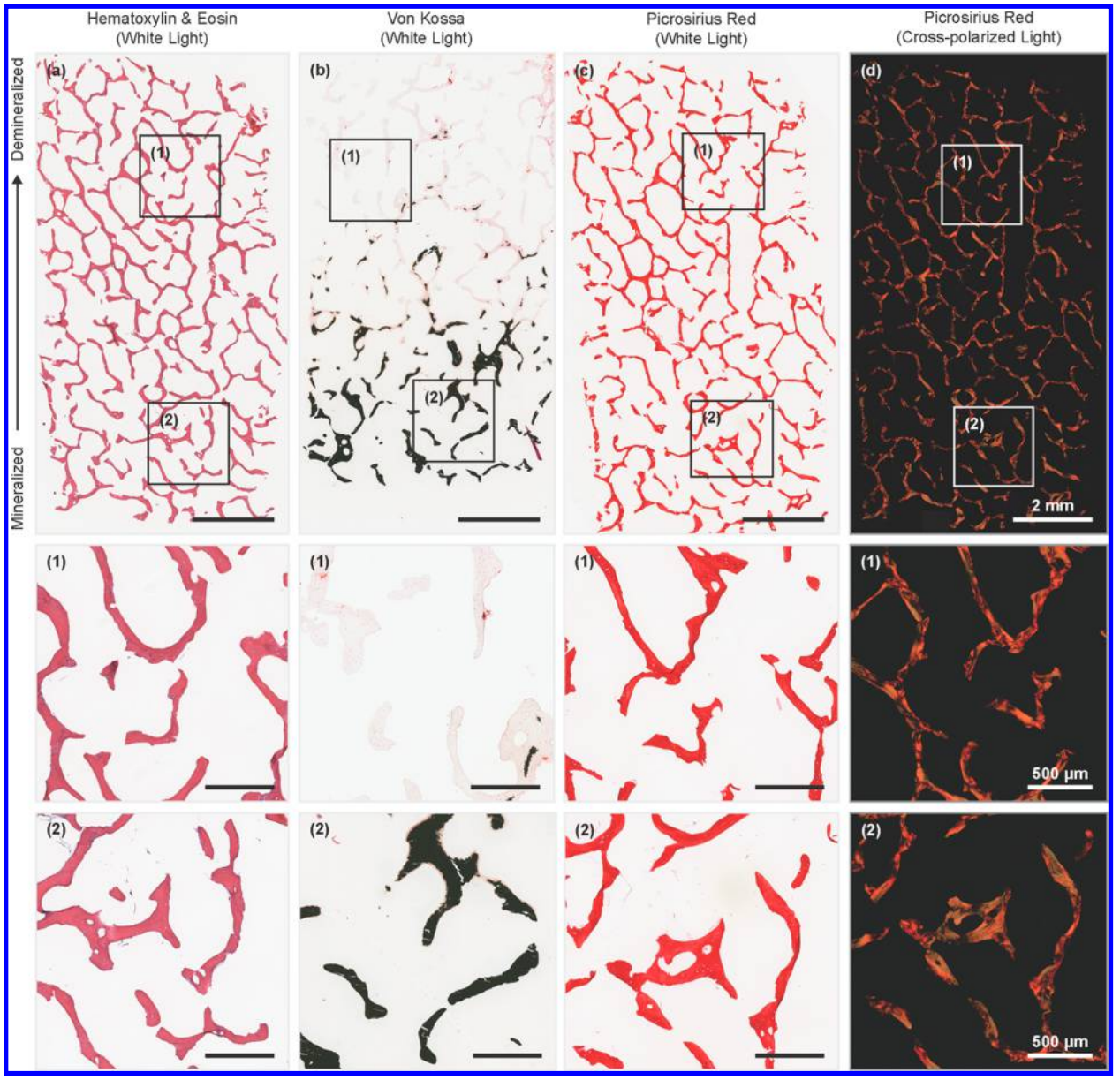

Figure 5. Histological stains for interfacial scaffolds, where parts a–d show the whole scaffold and parts 1 and 2 show insets from parts a–d. (a) Hematoxylin and eosin stain of the section. (b) Von Kossa stain of section. (c) Picrosirius Red stain of section under white light. (d) Same Picrosirius Red section under cross-polarizers.

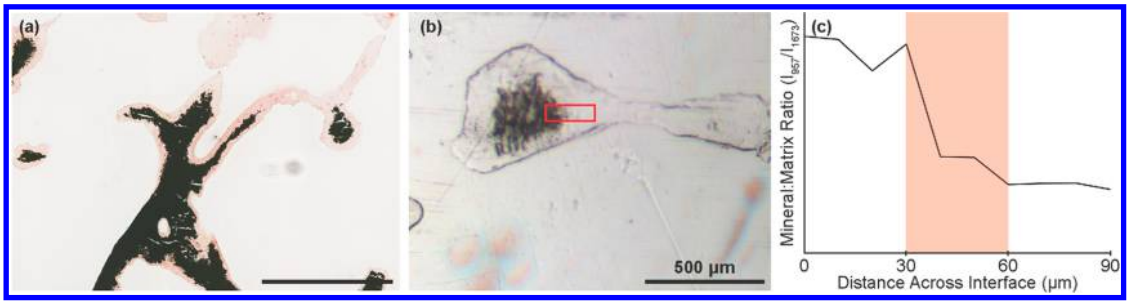

Figure 6. Images and Raman-derived line scan showing local compositional gradient within transitional zone between mineralized and demineralized tissue. (a) Von Kossa stain of transitional zone near the middle of a bone plug. (b) White light image showing a partially demineralized individual trabeculae. Red box indicates region from which a Raman line scan was collected. (c) Representative line scan of mineral:matrix ratio, derived from peak intensity ratio of 957 cm^{-1}:1673 cm^{-1} from Raman spectroscopy.

within the immediate transitional zone (Figure 6b,c, Figure S7). The size of this gradient was also confirmed by comparing these results to other mineral:matrix ratios (e.g., $\nu_2PO_4^{3-}$:amide I) as a function of distance.

DOI: 10.1021/acsbiomaterials.9b00176
ACS Biomater. Sci. Eng. 2019, 5, 2988–2997

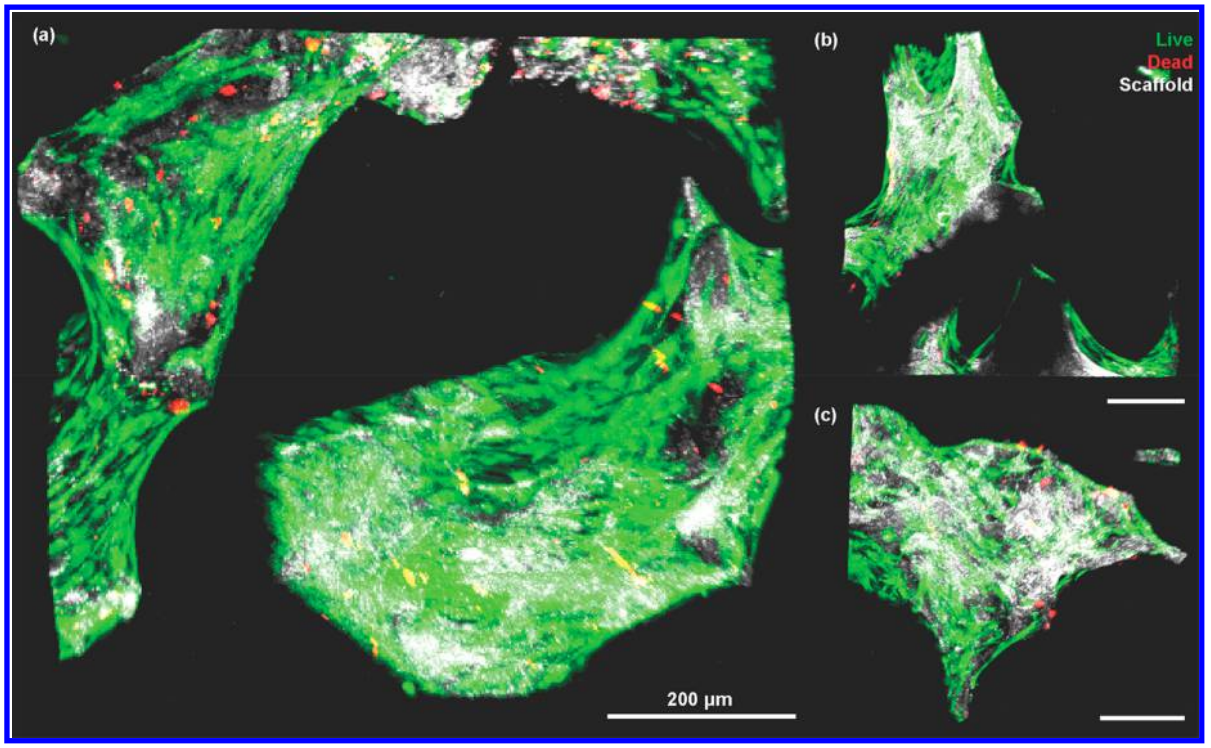

Figure 7. Live/dead stain of MSCs seeded onto interfacial scaffolds. Green indicates live cells. Red indicates dead cells, and white shows the scaffold through confocal reflectance. (a) Z-stack recorded from the center of the scaffold. (b) Z-stack recorded from demineralized end of scaffold. (c) Z-stack recorded from mineralized end of scaffold.

Finally, partially demineralized scaffolds were seeded with MSCs to confirm the applicability of these scaffolds for supporting cellular adhesion and growth. Live/dead staining (n = 6) of scaffolds found an average viability of 91% with no differences observed between the mineralized and demineralized ends of the scaffold (Figure S8). Cells were found to actively bind to the scaffold, spreading along the exterior of the trabeculae (Figure 7a, Figure S9). Qualitative differences in cell spreading were observed between the mineralized and demineralized portions of the scaffold (Figure 7b,c). To confirm this observation, samples were cultured for 4 days after seeding to determine the extent of this observation, and differences in cell spreading behavior on the demineralized portions of the scaffold versus the mineralized portions of the scaffold were observed (Figure S10). Cells appeared more elongated along the exterior of the trabeculae in the mineralized sections of the scaffold. Cells in the demineralized regions showed rounder phenotypes, grouping together in a matrix that the cells deposit around the scaffold (Figure S10).

DISCUSSION

We have demonstrated the fabrication of a native-like interfacial scaffold containing structural and compositional gradients of apatitic mineral using a spatially controlled, top-down approach. Studies have shown the feasibility of using decellularized scaffolds as implants,[4,5,7−9,31,39−41] but to the best of our knowledge, this study is the first to apply top-down approaches to biological systems in a spatially controlled manner. Given the inherent complexity of biological systems, top-down approaches are a useful mechanism for creating relevant systems for a variety of applications. The main challenge for this approach is identifying factors that vary within an animal population and that affect the resulting scaffold. We used neonatal bovine bone as a source of tissue, which provides a consistent source of tissue, but these explants show variation in the trabecular density. We were able to measure the trabecular density from our gradient scaffolds, finding that this factor is relevant to the overall demineralization of the scaffold (Figure 3). By measuring this property prior to beginning the demineralization process, a predictable gradient can be generated. Use of other tissues for top-down generation of tissue engineered scaffolds could be useful for a variety of applications, provided that the main variables are identified. For example, one could treat tendons using an enzymatic degradation to produce an oriented collagen scaffold that has a low enough density for cells to penetrate into the interior of the scaffold during seeding. These approaches will open up a new direction for future tissue engineering initiatives.

For generating a gradient in mineral content, we chose to use EDTA as demineralizing agent due to its chelating properties. Unlike harsher demineralizing agents such as HCl or formic acid, EDTA leaves the underlying protein matrix intact, allowing for a native-like scaffold.[30] Utilization of EDTA likely results in longer demineralization times than stronger acids, but these longer times provide more control over the demineralization process. Despite this factor, care still needs to be taken when applying the demineralizing fluid to the scaffolds. Any areas that are in contact with EDTA will demineralize, and improper application of the solution is likely to result in a fully demineralized scaffold. Utilizing this detail, however, means that the location of the mineral front can be easily controlled by modulating the point of contact between the scaffold and the demineralizing fluid (Figure S4). Utilization of this aspect allows the process to be modified for a multitude of applications.

DOI: 10.1021/acsbiomaterials.9b00176
ACS Biomater. Sci. Eng. 2019, 5, 2988−2997

We used pXRD to verify that the mineral type was not changed during demineralization of the scaffold. We observed peaks typically associated with the carbonated apatite found in bone (Figure 4). We also observed a peak at a 2θ of 8°, which is associated with the triple helical structure of collagen.[35] Interestingly, areas of the scaffold with a higher degree of demineralization also presented a higher intensity of the collagen helix peak as compared to mineralized areas of the scaffold. This increase in peak intensity may be related to a stress relaxation of the collagen in the scaffold as the intrafibrillar mineral platelets are removed from the collagen fibrils. A similar observation was found upon examination of Picrosirius Red stains of the collagen under cross-polarizers. Mineralized areas of the scaffold were found to have a green color, whereas demineralized areas of the scaffold were red. This green to red color change is related to an increase in the diameter and/or orientation of collagen.[36−38] As the demineralization process does not add any collagen to the scaffold, the diameter of the fibrils is unlikely to change. As such, this color change may be attributed to an increase in orientation, possibly related to the removal of internal stresses generated by the apatite platelets.

Our scaffolds contain a structural gradient extending across their length, continuously progressing from mineralized to demineralized tissue. If we focus on the transitional zone, we also observe a local compositional gradient across individual trabeculae (Figure 6a). Using Raman microscopy, we determined this gradient to be approximately 20−40 μm in length (Figure 6b,c and Figure S7), on the same order of magnitude as mineral:matrix gradients in native tissues.[42−44] Due to the presence of mineralized cores we observed in some trabeculae, we wanted to confirm that the gradient in the scaffolds is compositional, rather than a geometrical artifact resulting from this cored structure. As we observe a gradient that is longer than the thickness of the sections from which we collected the data, we believe this gradient is compositional. Further, as removal of mineral in our system progresses in a manner typical of any diffusion process, a compositional gradient at the scale of that found in native tissue is to be expected at the interface between mineralized and demineralized tissue. This gradient size makes these scaffolds ideal for examining cellular behavior at interfaces *in vitro*.

To examine the feasibility of using these scaffolds for tissue engineering applications, we seeded MSCs onto the scaffolds (Figure 7, Figure S9). We found high viability across the scaffold, with no observable difference in viability per location (mineralized or demineralized) (Figure S8). While the viability did not change as a function of location, the morphology of the cells did change from more elongated on the mineralized sections to more rounded on the demineralized sections. These morphological differences are most likely in response to changes in material properties, such as stiffness, between these areas.[45,46] More analysis, however, needs to be performed to confirm that these observations relate to scaffold-driven differentiation of the seeded cells.

Our synthetic approach results in a scaffold possessing compositional and hierarchical structuring similar to that observed in native tissues. Significantly, a key feature of the scaffolds prepared using this top-down approach is that the collagen network remains continuous throughout the entire length of the scaffold. This feature is critical for ensuring a mechanically robust scaffold. Our scaffolds, however, do not possess the interfacial regions present in the osteochondral interface, enthesis, or growth plate. Despite the lack of native morphology, our scaffolds are porous and thus can be easily integrated with injectable materials, such as collagen gels, with and without cells. Previous experiments from our laboratories using fully mineralized bone biopsies have shown promise for direct interaction between reconstituted collagen gels and the cell-deposited matrix surrounding the bone scaffold.[32]

These scaffolds have applications in a variety of fields that target the construction of interfacial biological systems through tissue engineering. Orthopedic tissue interfaces, such as the enthesis or the osteochondral interface, require the presence of a mineral gradient to function.[10−12] For example, these scaffolds could be applied to systems that use similar tissues to generate seamless interfacial structures.[32] These scaffolds would also be useful for analyzing cellular behavior in developmental systems. For example, seeding chondrocytes or other musculoskeletal cells onto interfacial scaffolds would allow for the *in vitro* study of cellular behavior during endochondral ossification or long bone growth directed from the growth plate. Our partially mineralized scaffolds are also useful for examining cellular behavior in pathological systems. For example, the growth plate has been implicated as a possible "metastatic niche" for cancer cell localization.[21] Interfacial scaffolds allow for the direct study of these systems without requiring complex animal models. Further, scaffolds containing both mineralized and unmineralized regions allow for studying cell behaviors as a function of material composition, which can be useful when assessing the potential of particular cancer cells to metastasize to bone.

In conclusion, we successfully fabricated a hierarchically structured scaffold containing structural and compositional mineral gradients for use in tissue engineering. This scaffold was created using a top-down approach that has not previously been applied to biological systems. These scaffolds were shown to contain a gradient in mineral content using a combination of μCT, pXRD, histology, and Raman microscopy, and the resulting scaffolds were found to be compatible with typical cell seeding methodologies. The scaffolds will be useful for a variety of tissue engineering applications, targeting the complex interfacial systems found in biology. Further, the top-down approach to tissue engineering provides access to a wider range of tissue morphologies and hierarchies than previously accessible.

■ ASSOCIATED CONTENT

Supporting Information

The Supporting Information is available free of charge on the ACS Publications website at DOI: 10.1021/acsbiomaterials.9b00176.

Supplemental methods, calculation of scaffold length, μCT renderings of scaffolds, alternate views of demineralization model, Raman microscopic data showing mineral:matrix gradients, cell viability plot, alternate view of live/dead images, and histology of seeded scaffolds (PDF)

Movie 1 showing μCT rendering of scaffold (AVI)

■ AUTHOR INFORMATION

Corresponding Authors

*E-mail: lae37@cornell.edu. Phone: (607) 254-5256.
*E-mail: lb244@cornell.edu. Phone: (607) 255-9381.

DOI: 10.1021/acsbiomaterials.9b00176
ACS Biomater. Sci. Eng. 2019, 5, 2988−2997

ORCID

Alexander J. Boys: 0000-0002-6488-7005
Lara A. Estroff: 0000-0002-7658-1265

Notes

The authors declare no competing financial interest.

■ ACKNOWLEDGMENTS

We would like to acknowledge Jennie A. M. R. Kunitake and Tianyu Gao for their assistance in running and analyzing the Raman experiments in this study. A.J.B. acknowledges a predoctoral fellowship award (F31AR070009) from the National Institute of Arthritis and Musculoskeletal and Skin Diseases (NIAMS) of the National Institutes of Health (NIH). The content is solely the responsibility of the authors and does not necessarily represent the official views of the National Institutes of Health. We also acknowledge Cornell Center for Materials Research (CCMR) under DMR-1719875 for instrument usage, the Cornell University College of Veterinary Medicine for histological embedding and sectioning, and the Cornell University Biotechnology Resource Center (BRC) for instruments usage under Grants NIH S10RR025502 and NIH S10OD012287. We also acknowledge the Yale University Bone Histology and Histomorphometry Laboratory for histological embedding and sectioning.

■ REFERENCES

(1) Kataoka, K.; Harada, A.; Nagasaki, Y. Block copolymer micelles for drug delivery: Design, characterization and biological significance. *Adv. Drug Delivery Rev.* **2012**, *64*, 37−48.
(2) Murphy, S. V.; Atala, A. 3D bioprinting of tissues and organs. *Nat. Biotechnol.* **2014**, *32* (8), 773−785.
(3) Pham, Q. P.; Sharma, U.; Mikos, A. G. Electrospinning of Polymeric Nanofibers for Tissue Engineering Applications: A Review. *Tissue Eng.* **2006**, *12* (5), 1197−1211.
(4) Voytik-Harbin, S. L.; Brightman, A. O.; Kraine, M. R.; Waisner, B.; Badylak, S. F. Identification of extractable growth factors from small intestinal submucosa. *J. Cell. Biochem.* **1997**, *67* (4), 478−491.
(5) Badylak, S. F.; Tullius, R.; Kokini, K.; Shelbourne, K. D.; Klootwyk, T.; Voytik, S. L.; Kraine, M. R.; Simmons, C. The use of xenogeneic small intestinal submucosa as a biomaterial for Achille's tendon repair in a dog model. *J. Biomed. Mater. Res.* **1995**, *29* (8), 977−985.
(6) Badylak, S.; Kokini, K.; Tullius, B.; Simmons-Byrd, A.; Morff, R. Morphologic study of small intestinal submucosa as a body wall repair device. *J. Surg. Res.* **2002**, *103* (2), 190−202.
(7) Badylak, S. F.; Lantz, G. C.; Coffey, A.; Geddes, L. A. Small Intestinal Submucosa as a Large Diameter Vascular Graft in the Dog. *J. Surg. Res.* **1989**, *47* (1), 74−80.
(8) Gruskin, E.; Doll, B. A.; Futrell, F. W.; Schmitz, J. P.; Hollinger, J. O. Demineralized bone matrix in bone repair: History and use. *Adv. Drug Delivery Rev.* **2012**, *64* (12), 1063−1077.
(9) Finkemeier, C. G. Bone-Grafting and Bone-Graft Substitutes. *J. Bone Jt. Surg.* **2002**, *84* (3), 454−464.
(10) Boys, A. J.; McCorry, M. C.; Rodeo, S. A.; Bonassar, L. J.; Estroff, L. A. Next generation tissue engineering of orthopedic soft tissue-to-bone interfaces. *MRS Commun.* **2017**, *7* (3), 289−308.
(11) Bonnevie, E. D.; Mauck, R. L. Physiology and Engineering of the Graded Interfaces of Musculoskeletal Junctions. *Annu. Rev. Biomed. Eng.* **2018**, *20*, 403−429.
(12) Lu, H. H.; Thomopoulos, S. Functional attachment of soft tissues to bone: development, healing, and tissue engineering. *Annu. Rev. Biomed. Eng.* **2013**, *15*, 201−226.
(13) Weiner, S.; Wagner, H. D. The Material Bone: Structure-Mechanical Function Relations. *Annu. Rev. Mater. Sci.* **1998**, *28*, 271−298.
(14) Reznikov, N.; Shahar, R.; Weiner, S. Bone hierarchical structure in three dimensions. *Acta Biomater.* **2014**, *10*, 3815−3826.
(15) Reznikov, N.; Bilton, M.; Lari, L.; Stevens, M. M.; Kröger, R. Fractal-like hierarchical organization of bone begins at the nanoscale. *Science* **2018**, *360*, eaao2189.
(16) Yang, P. J.; Temenoff, J. S. Engineering orthopedic tissue interfaces. *Tissue Eng., Part B* **2009**, *15* (2), 127−141.
(17) Font Tellado, S.; Balmayor, E. R.; Van Griensven, M. Strategies to engineer tendon/ligament-to-bone interface: Biomaterials, cells and growth factors. *Adv. Drug Delivery Rev.* **2015**, *94*, 126.
(18) Mente, P. L.; Lewis, J. L. Elastic modulus of calcified cartilage is an order of magnitude less than that of subchondral bone. *J. Orthop. Res.* **1994**, *12* (5), 637−647.
(19) Abraham, A. C.; Haut Donahue, T. L. From meniscus to bone: A quantitative evaluation of structure and function of the human meniscal attachments. *Acta Biomater.* **2013**, *9* (5), 6322−6329.
(20) Goldring, M. B.; Tsuchimochi, K.; Ijiri, K. The control of chondrogenesis. *J. Cell. Biochem.* **2006**, *97* (1), 33−44.
(21) He, F.; Chiou, A. E.; Loh, H. C.; Lynch, M.; Seo, B. R.; Song, Y. H.; Lee, M. J.; Hoerth, R.; Bortel, E. L.; Willie, B. M.; et al. Multiscale characterization of the mineral phase at skeletal sites of breast cancer metastasis. *Proc. Natl. Acad. Sci. U. S. A.* **2017**, *114*, 10542.
(22) Choi, S.; Friedrichs, J.; Song, Y. H.; Werner, C.; Estroff, L. A.; Fischbach, C. Intrafibrillar, bone-mimetic collagen mineralization regulates breast cancer cell adhesion and migration. *Biomaterials* **2019**, *198*, 95.
(23) Spalazzi, J. P.; Doty, S. B.; Moffat, K. L.; Levine, W. N.; Lu, H. H. Development of controlled matrix heterogeneity on a triphasic scaffold for orthopedic interface tissue engineering. *Tissue Eng.* **2006**, *12* (12), 3497−3508.
(24) Ma, J.; Smietana, M. J.; Kostrominova, T. Y.; Wojtys, E. M.; Larkin, L. M.; Arruda, E. M. Three-Dimensional Engineered Bone−Ligament−Bone Constructs for Anterior Cruciate Ligament Replacement. *Tissue Eng., Part A* **2012**, *18* (1−2), 103−116.
(25) Font Tellado, S.; Bonani, W.; Balmayor, E. R.; Föhr, P.; Motta, A.; Migliaresi, C.; van Griensven, M. Fabrication and characterization of biphasic silk fibroin scaffolds for tendon/ligament-to-bone tissue engineering. *Tissue Eng., Part A* **2017**, *23* (15−16), 859−872.
(26) Liu, W.; Lipner, J.; Xie, J.; Manning, C. N.; Thomopoulos, S.; Xia, Y. Nano fiber Scaffolds with Gradients in Mineral Content for Spatial Control of Osteogenesis. *ACS Appl. Mater. Interfaces* **2014**, *6*, 2842−2849.
(27) Lin, H.; Lozito, T. P.; Alexander, P. G.; Gottardi, R.; Tuan, R. S. Stem Cell-Based Microphysiological Osteochondral System to Model Tissue Response to Interleukin-1 β. *Mol. Pharmaceutics* **2014**, *11*, 2203−2212.
(28) Lipner, J.; Liu, W.; Liu, Y. X.; Boyle, J.; Genin, G. M.; Xia, Y.; Thomopoulos, S. The mechanics of PLGA nanofiber scaffolds with biomimetic gradients in mineral for tendon-to-bone repair. *J. Mech. Behav. Biomed. Mater.* **2014**, *40*, 59−68.
(29) Zhu, C.; Qiu, J.; Pongkitwitoon, S.; Thomopoulos, S.; Xia, Y. Inverse Opal Scaffolds with Gradations in Mineral Content for Spatial Control of Osteogenesis. *Adv. Mater.* **2018**, *30* (29), 1706706.
(30) Quan, B. D.; Sone, E. D. Structural changes in collagen fibrils across a mineralized interface revealed by cryo-TEM. *Bone* **2015**, *77*, 42−49.
(31) McCorry, M. C.; Mansfield, M. M.; Sha, X.; Coppola, D. J.; Lee, J. W.; Bonassar, L. J. A model system for developing a tissue engineered meniscal enthesis. *Acta Biomater.* **2017**, *56*, 110−117.
(32) Iannucci, L. E.; Boys, A. J.; McCorry, M. C.; Estroff, L. A.; Bonassar, L. J. Cellular and Chemical Gradients to Engineer the Meniscus-to-Bone Insertion. *Adv. Healthcare Mater.* **2019**, *8*, 1800806.
(33) Schindelin, J.; Arganda-carreras, I.; Frise, E.; Kaynig, V.; Longair, M.; Pietzsch, T.; Preibisch, S.; Rueden, C.; Saalfeld, S.; Schmid, B.; et al. Fiji: an open-source platform for biological-image analysis. *Nat. Methods* **2012**, *9* (7), 676−682.
(34) Talari, A. C. S.; Movasaghi, Z.; Rehman, S.; Rehman, I. U. Raman spectroscopy of biological tissues. *Appl. Spectrosc. Rev.* **2015**, *50*, 46−111.

DOI: 10.1021/acsbiomaterials.9b00176
ACS Biomater. Sci. Eng. 2019, 5, 2988−2997

(35) Nicoletti, A.; Torricelli, P.; Bigi, A.; Fornasari, P.; Fini, M.; Moroni, L. Incorporation of nanostructured hydroxyapatite and poly(N -isopropylacrylamide) in demineralized bone matrix enhances osteoblast and human mesenchymal stem cell activity. *Biointerphases* **2015**, *10* (4), No. 041001.
(36) Junqueira, L. C.; Bignolas, G.; Brentani, R. R. Picrosirius staining plus polarization microscopy, a specific method for collagen detection in tissue sections. *Histochem. J.* **1979**, *11*, 447−455.
(37) Rich, L.; Whittaker, P. Collagen and Picrosirius Red Staining: a Polarized Light Assessment of Fibrillar Hue and Spatial Distribution. *Brazilian J. Morphol. Sci.* **2005**, *22* (2), 97−104.
(38) Dayan, D.; Hiss, Y.; Hirshberg, A.; Bubis, J. J.; Wolman, M. Are the polarization colors of picrosirius red-stained collagen determined only by the diameter of the fibers? *Histochemistry* **1989**, *93*, 27−29.
(39) Grayson, W. L.; Fröhlich, M.; Yeager, K.; Bhumiratana, S.; Chan, M. E.; Cannizzaro, C.; Wan, L. Q.; Liu, X. S.; Guo, X. E.; Vunjak-Novakovic, G. Engineering anatomically shaped human bone grafts. *Proc. Natl. Acad. Sci. U. S. A.* **2010**, *107* (8), 3299−3304.
(40) Grayson, W. L.; Bhumiratana, S.; Grace Chao, P. H.; Hung, C. T.; Vunjak-Novakovic, G. Spatial regulation of human mesenchymal stem cell differentiation in engineered osteochondral constructs: Effects of pre-differentiation, soluble factors and medium perfusion. *Osteoarthr. Cartil.* **2010**, *18* (5), 714−723.
(41) Grayson, W. L.; Bhumiratana, S.; Cannizzaro, C.; Chao, P. G.; Lennon, D. P.; Caplan, A. I.; Vunjak-Novakovic, G. Effects of Initial Seeding Density and Fluid Perfusion Rate on Formation of Tissue-Engineered Bone. *Tissue Eng., Part A* **2008**, *14* (11), 1809−1820.
(42) Schwartz, A. G.; Pasteris, J. D.; Genin, G. M.; Daulton, T. L.; Thomopoulos, S. Mineral Distributions at the Developing Tendon Enthesis. *PLoS One* **2012**, *7* (11), e48630.
(43) Deymier-Black, A. C.; Pasteris, J. D.; Genin, G. M.; Thomopoulos, S. Allometry of the Tendon Enthesis: Mechanisms of Load Transfer Between Tendon and Bone. *J. Biomech. Eng.* **2015**, *137* (11), 111005.
(44) Deymier, A. C.; An, Y.; Boyle, J. J.; Schwartz, A. G.; Birman, V.; Genin, G. M.; Thomopoulos, S.; Barber, A. H. Micro-mechanical Properties of the Tendon-to-Bone Attachment. *Acta Biomater.* **2017**, *56*, 25−35.
(45) Mao, A. S.; Shin, J. W.; Mooney, D. J. Effects of substrate stiffness and cell-cell contact on mesenchymal stem cell differentiation. *Biomaterials* **2016**, *98*, 184−191.
(46) Chaudhuri, O.; Gu, L.; Klumpers, D.; Darnell, M.; Bencherif, S. A.; Weaver, J. C.; Huebsch, N.; Lee, H. P.; Lippens, E.; Duda, G. N.; et al. Hydrogels with tunable stress relaxation regulate stem cell fate and activity. *Nat. Mater.* **2016**, *15* (3), 326−334.

DOI: 10.1021/acsbiomaterials.9b00176
ACS Biomater. Sci. Eng. 2019, 5, 2988−2997